Electronic Supplementary Material (ESI) for Journal of Materials Chemistry A.

Supporting Information

Charge Modulation Over Atomically Precise Metal Nanoclusters via Non-conjugated Polymer for Photoelectrochemical Water Oxidation

Yang Xiao[a], Qiao-Ling Mo[a], Gao Wu[a], Kun Wang[a], Xing-Zu Ge[a], Shu-Ran Xu[a], Jia-Le Li[a], Yue Wu*[a], Fang-Xing Xiao*[ab]

a. College of Materials Science and Engineering, Fuzhou University, New Campus, Minhou, Fujian Province, 350108, China.

b. Fujian Science & Technology Innovation Laboratory for Optoelectronic Information of China, Fuzhou, Fujian 350108, P. R. China.

E-mail: yue_wu@fzu.edu.cn

fxxiao@fzu.edu.cn

Experimental Section

1. Materials

Titanium sheet (99.99%, 0.1×20×50 mm), Graphite sheet (99.6%), Deionized water (DI H_2O, Millipore, 18.2MΩ cm resistivity), Ethylene glycol ($C_2H_6O_2$), Ammonia fluoride (NH_4F), Hydrogen fluoride (HF), Nitric acid (HNO_3), Sodium hydroxide (NaOH), Sodium sulfate (Na_2SO_4), hydrochloric acid (HCl), ammonium oxalate ($(NH_4)_2C_2O_4$), Sodium borohydride ($NaBH_4$), Silver nitrate ($AgNO_3$), gold (III) chloride trihydrate ($HAuCl_4 \cdot 3H_2O$) were obtained from Sinopharm Chemical Reagent Co., Ltd (Shanghai, China). L-glutathione (GSH) and poly (allylamine hydrochloride) (PAH, average Mw=17.5 kDa) were obtained from Sigma-Aldrich. All reagents above were used as received without further purification.

2. Preparation of TiO_2 nanotube arrays (TNTAs) [1]

Ti foil was first thoroughly sonicated in acetone, ethanol and DI H_2O for 15 min, respectively. Then, Ti sheets were immersed in a mixed solution of HF-HNO_3-H_2O with volume ratio of 1 : 4 : 5 for 20 s, washed by DI H_2O and dried with a gentle N_2 stream. Anodization was carried out under ambient conditions at 50 V for 2 h with ca. 3 cm separation distance between the working (Ti foil) and counter electrode (graphite). The electrolyte consists of 0.3 wt % of NH_4F (0.6 g) in ethylene glycol (196 mL) and DI H_2O (4 mL). After the first-step anodization, the as-obtained TiO_2 layer was removed from Ti foil by sonication in ethanol for 5 min, washed by DI H_2O and dried with a N_2 stream. The second anodization was performed at 50 V for 30 min to produce the TNTAs. Similarly, the resulting TNTAs were also washed by DI H_2O, dried with a N_2 stream and finally calcined at 450 ℃ for 3 h in air with a heating rate of 5 ℃ min^{-1}.

3. Preparation of Au_x@GSH nanoclusters (NCs)[2]

$HAuCl_4 \cdot 3H_2O$ (40 mg) and L-glutathione (GSH, 46 mg) were thoroughly mixed in 50 mL of DI H2O at ambient conditions. The mixture was continuously stirred until the appearance of a colorless solution and then was heated at 70 °C for 24 h. Subsequently, the Au_x@GSH NCs aqueous solution was stored in a refrigerator at 4 °C for further use.

4. Preparation of Au_{25}@$(GSH)_{18}$ NCs [2]

A mixture of glutathione-protected Au nanoclusters was synthesized according to the literature with some modifications. Briefly, L-glutathione (GSH, reduced form, 1 mmol) was added to methanol (50mL) containing $HAuCl_4 \cdot 3H_2O$ (0.25 mmol). Under vigorous stirring, an ice-cold $NaBH_4$ aqueous solution (0.2

M, 12.5 mL) was added and aged for 1 h. The obtained precipitate was thoroughly washed with methanol and dried in vacuum at room temperature to obtain a mixture of Au clusters. The mixture (49 mg) was dissolved in an aqueous solution (70 mL) containing GSH (1.307 g) and stirred at 55 °C under air bubbling for 6-9 h to obtain $Au_{25}@(GSH)_{18}$ NCs. To remove excess GSH, the obtained solution containing the $Au_{25}@(GSH)_{18}$ NCs was loaded into a dialysis membrane (MW 8000) and stirred slowly at room temperature for 12 h. The precipitate formed during dialysis was removed with a filter (pore size, 0.2μm). It was confirmed by polyacrylamide gel electrophoresis that the obtained solution contains no other clusters.

5. Preparation of Ag_x@GSH NCs reference[3]

Firstly, 12.5 mL of 20 mM $AgNO_3$ and 7.5 mL of 50 mM reduced-glutathione (GSH) were added to a 500 mL flask containing 200 mL of ultrapure water. Stirring the white precipitates for 2 min, and then changing the pH of the reaction mixture to 11 by adding a 1 M NaOH solution. Subsequently, heating this solution at 90 °C for 1 h under stirring at 500 rpm. After the solution was naturally cooled to room temperature, the pH was changed again to 3.75 by adding 1 M HCl. Finally, the NC solution was aged for 24h at room temperature, and all precipitates appeared during this period were removed via centrifugation.

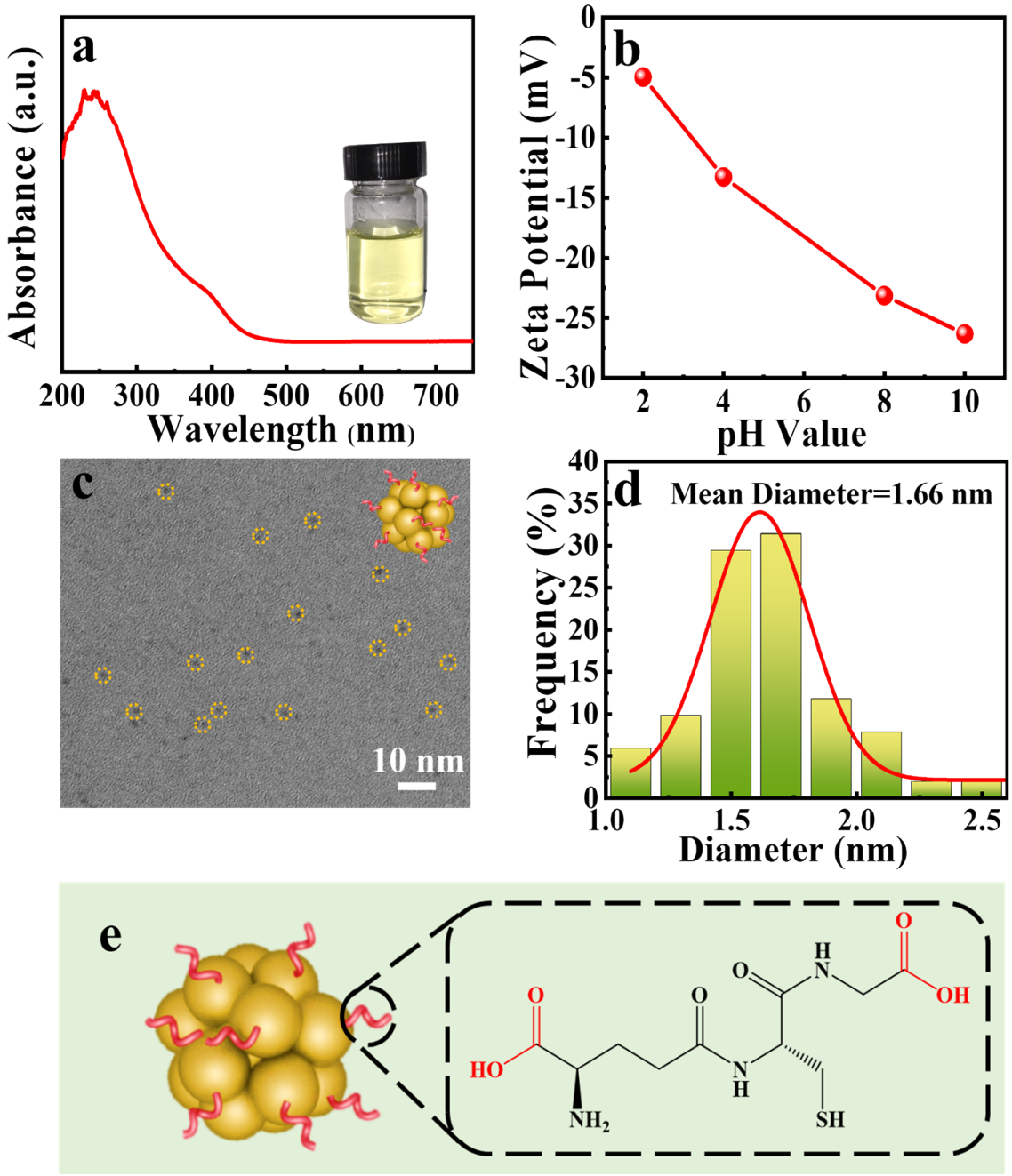

Figure S1. (a) UV-vis absorption spectrum, (b) Zeta potential, (c) TEM image, (d) size distribution histogram of Au_x@GSH NCs and (e) GSH model.

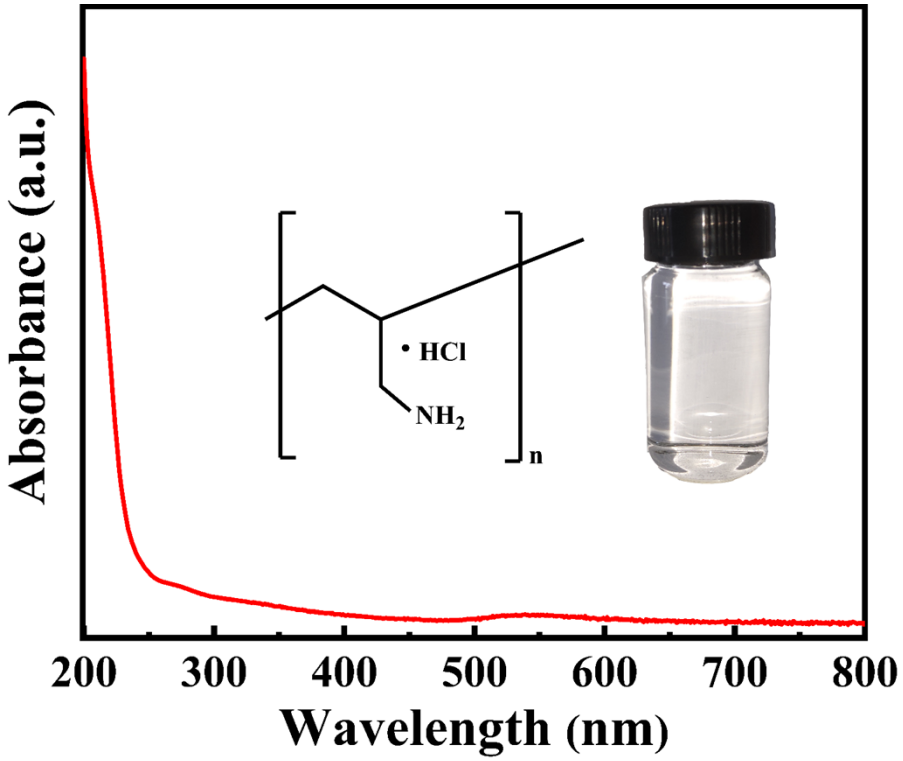

Figure S2. UV-vis absorption spectrum of PAH aqueous solution with photograph and molecular structures in the inset.

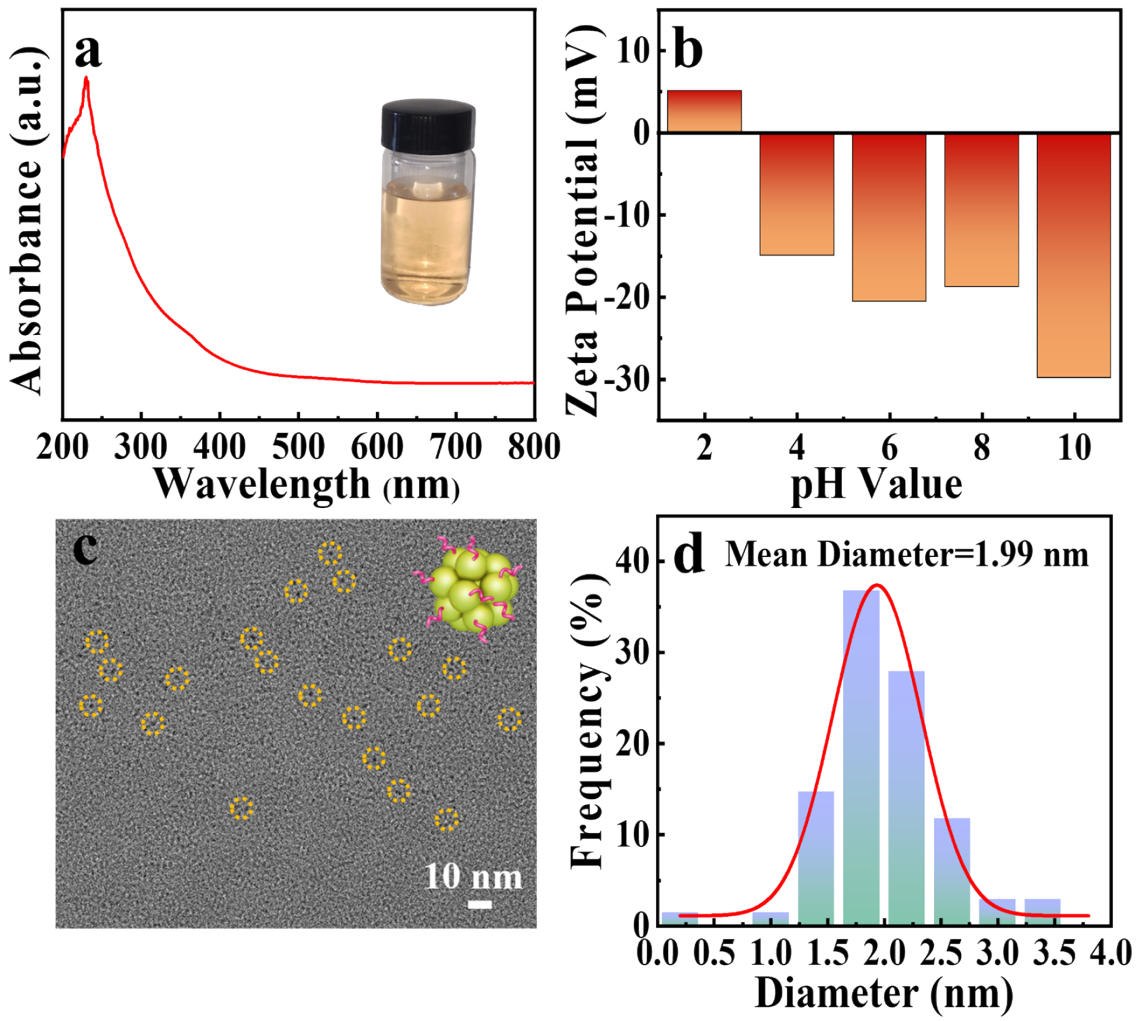

Figure S3. (a) UV-vis absorption spectrum, (b) Zeta potential, (c) TEM image and (d) size distribution histogram of Ag_x@GSH NCs.

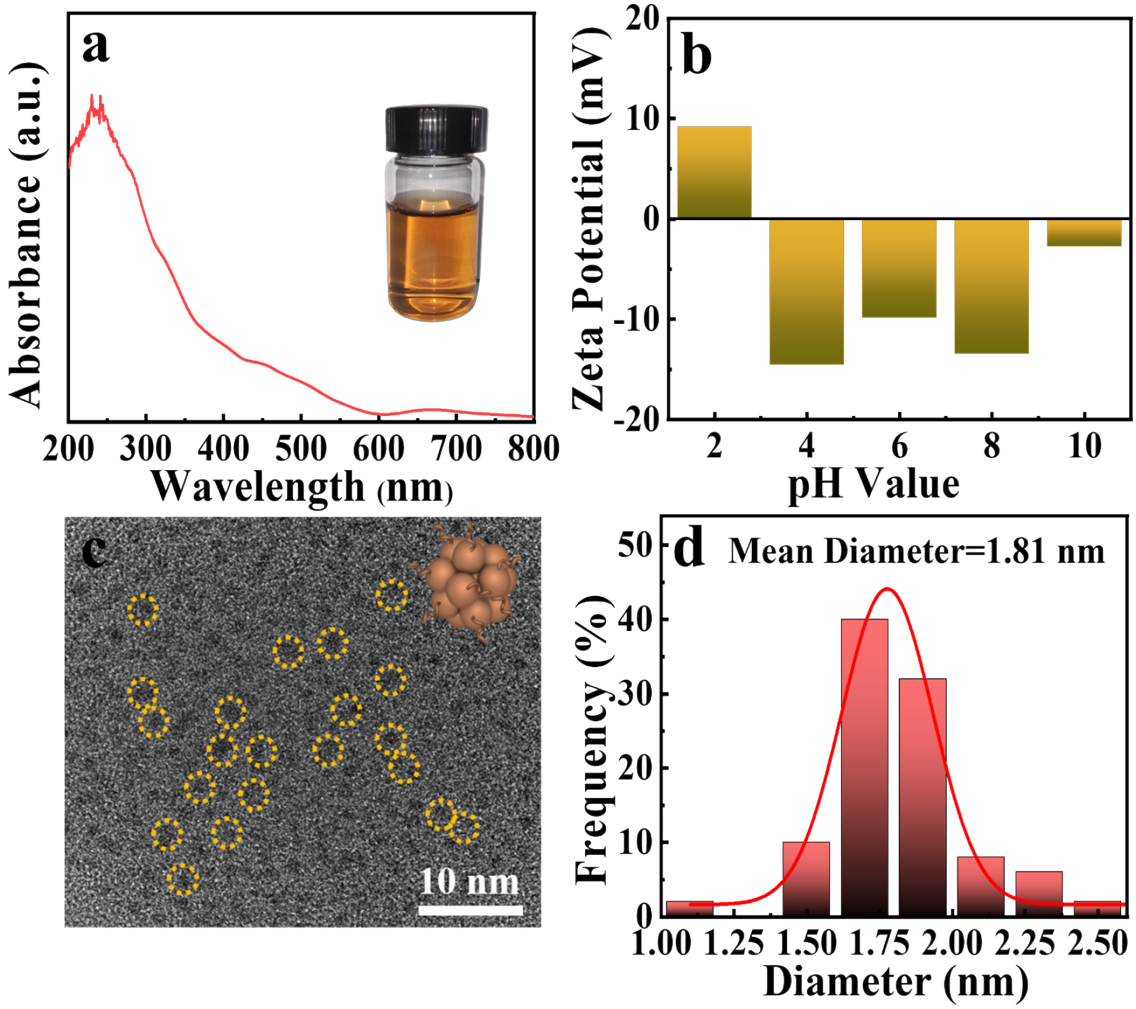

Figure S4. (a) UV-vis absorption spectrum, (b) Zeta potential, (c) TEM image and (d) size distribution histogram of Au_{25}@GSH_{18} NCs.

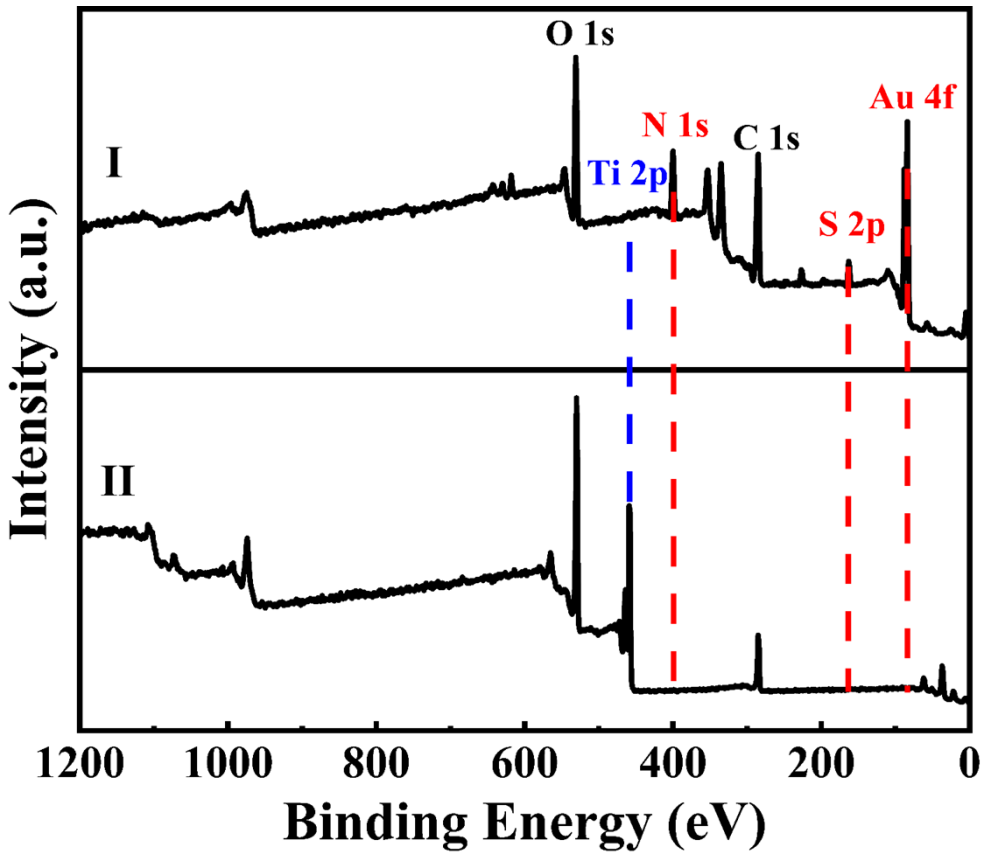

Figure S5. Survey spectra of (I) $T(Au_xP)_8$ (II) TNTAs.

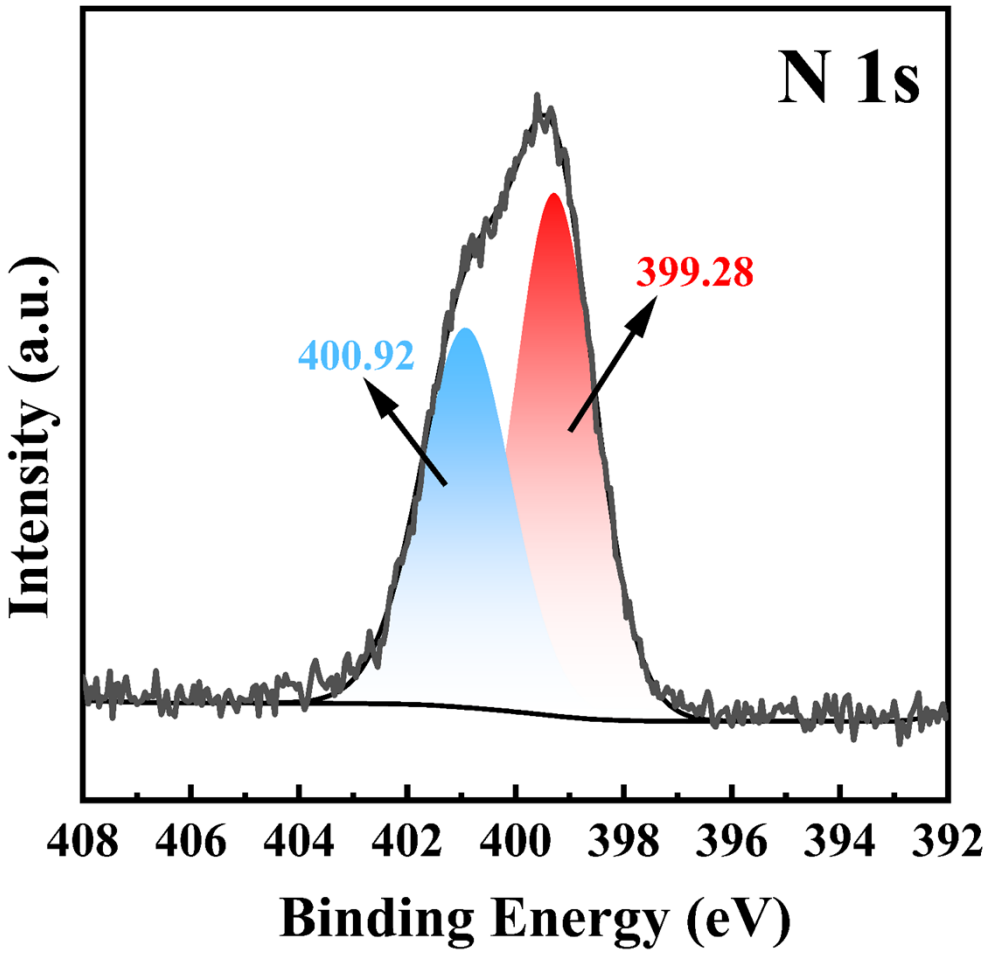

Figure S6. High-resolution (d) N 1s spectra of $T(Au_xP)_8$.

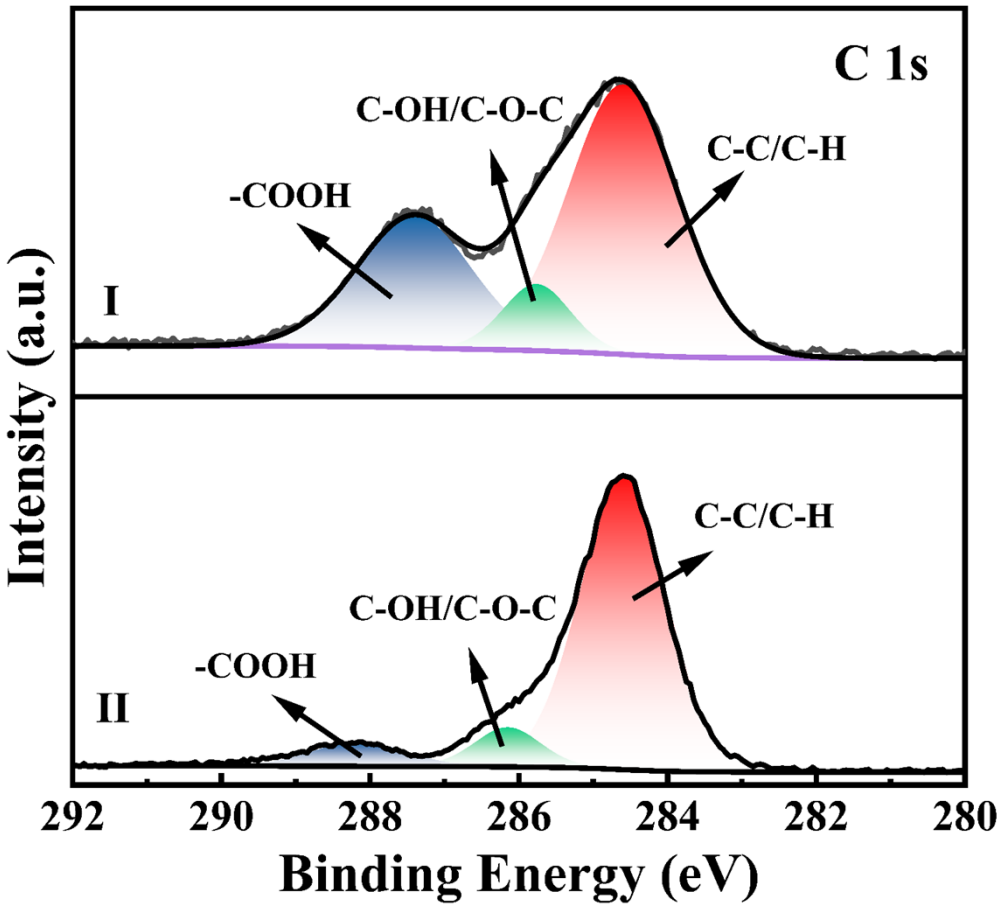

Figure S7. High-resolution C 2s spectra of (I) $T(Au_xP)_8$ and (II) blank TNTAs.

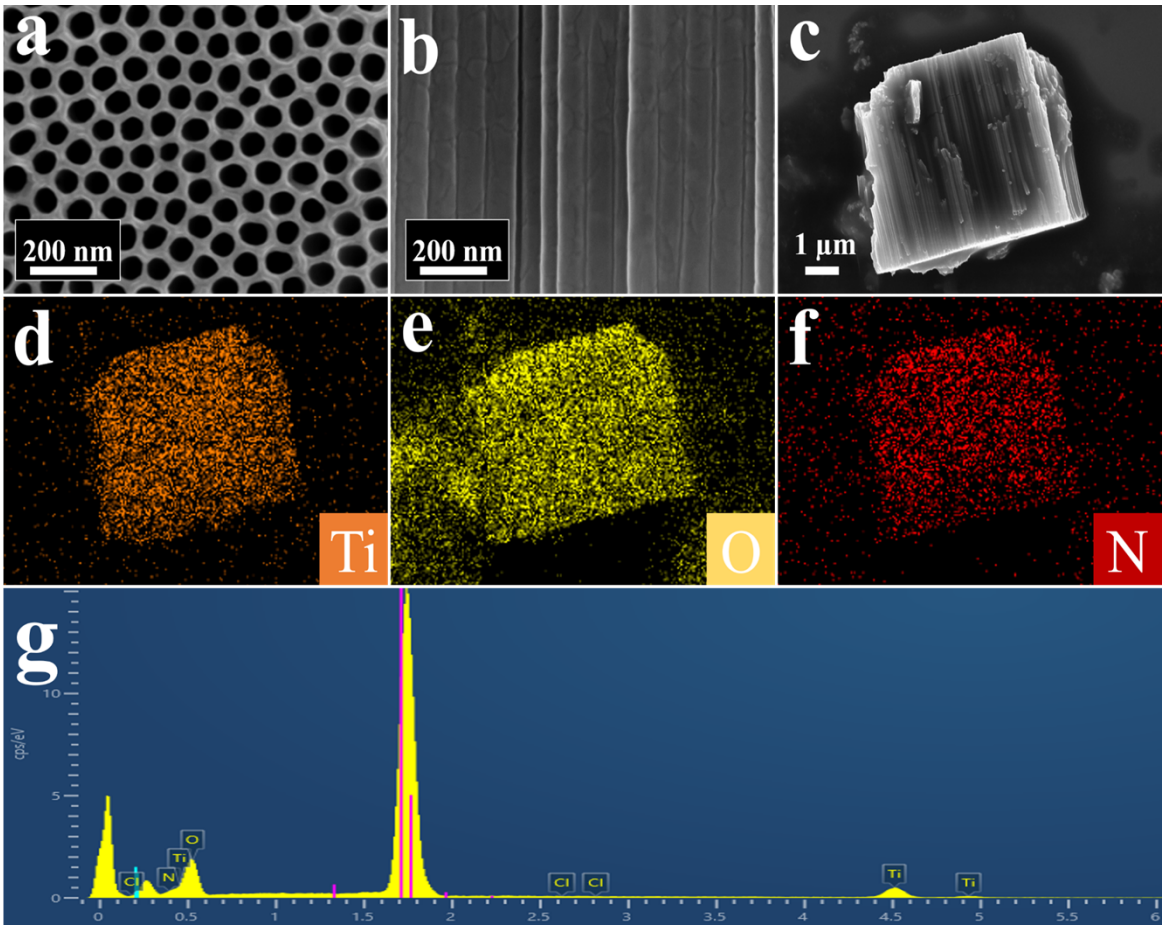

Figure S8. (a-b) Top-view and cross-sectional FESEM images of TP_8 heterostructure, (c) low-magnification FESEM image with corresponding (d–f) elemental mapping and (h) EDS results.

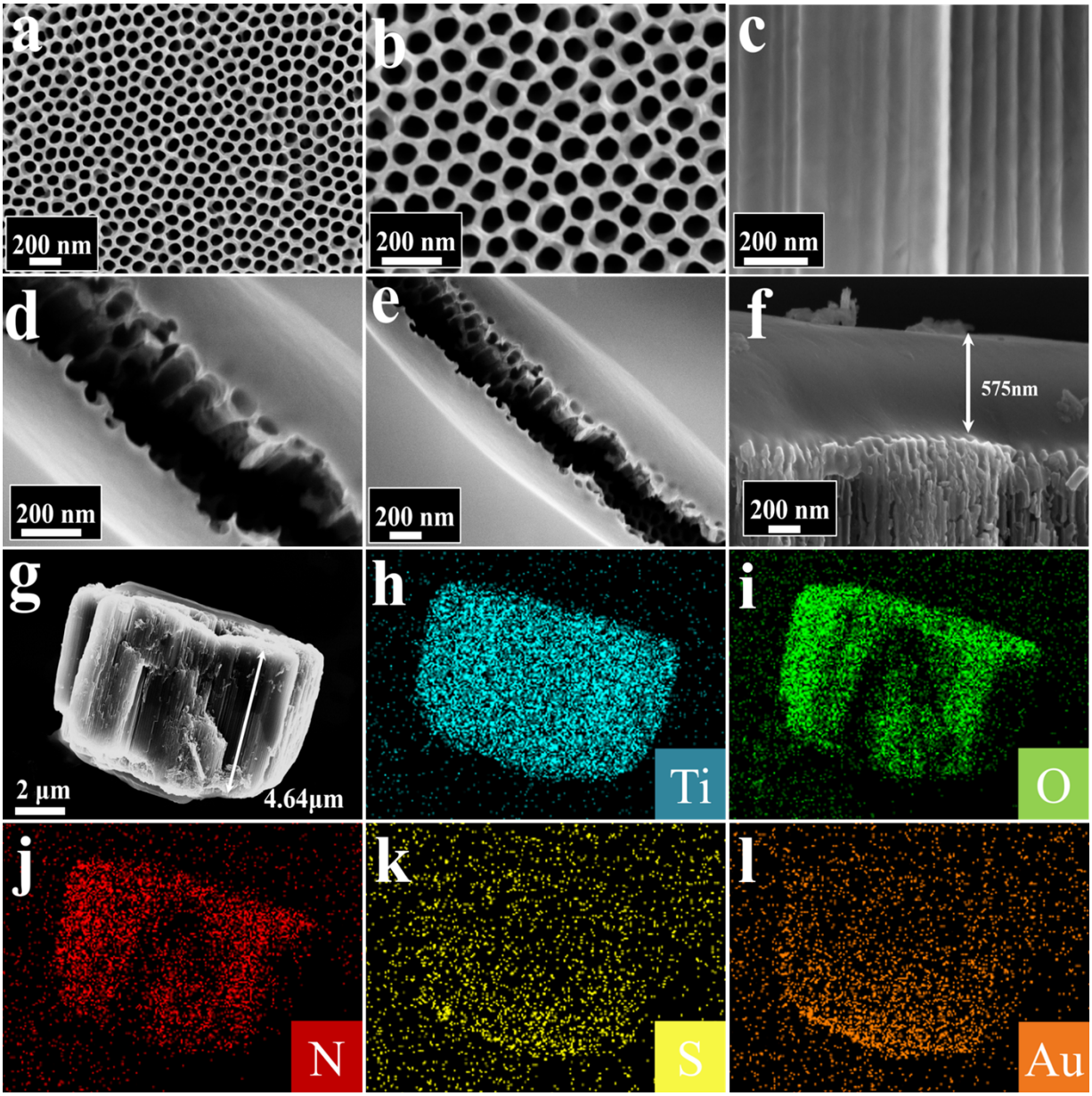

Figure S9. Top-view and cross-sectional FESEM images of (a-c) blank TNTAs and (d-f) $T(Au_xP)_8$ heterostructure, (g) low-magnification FESEM image with corresponding (h–l) elemental mapping results.

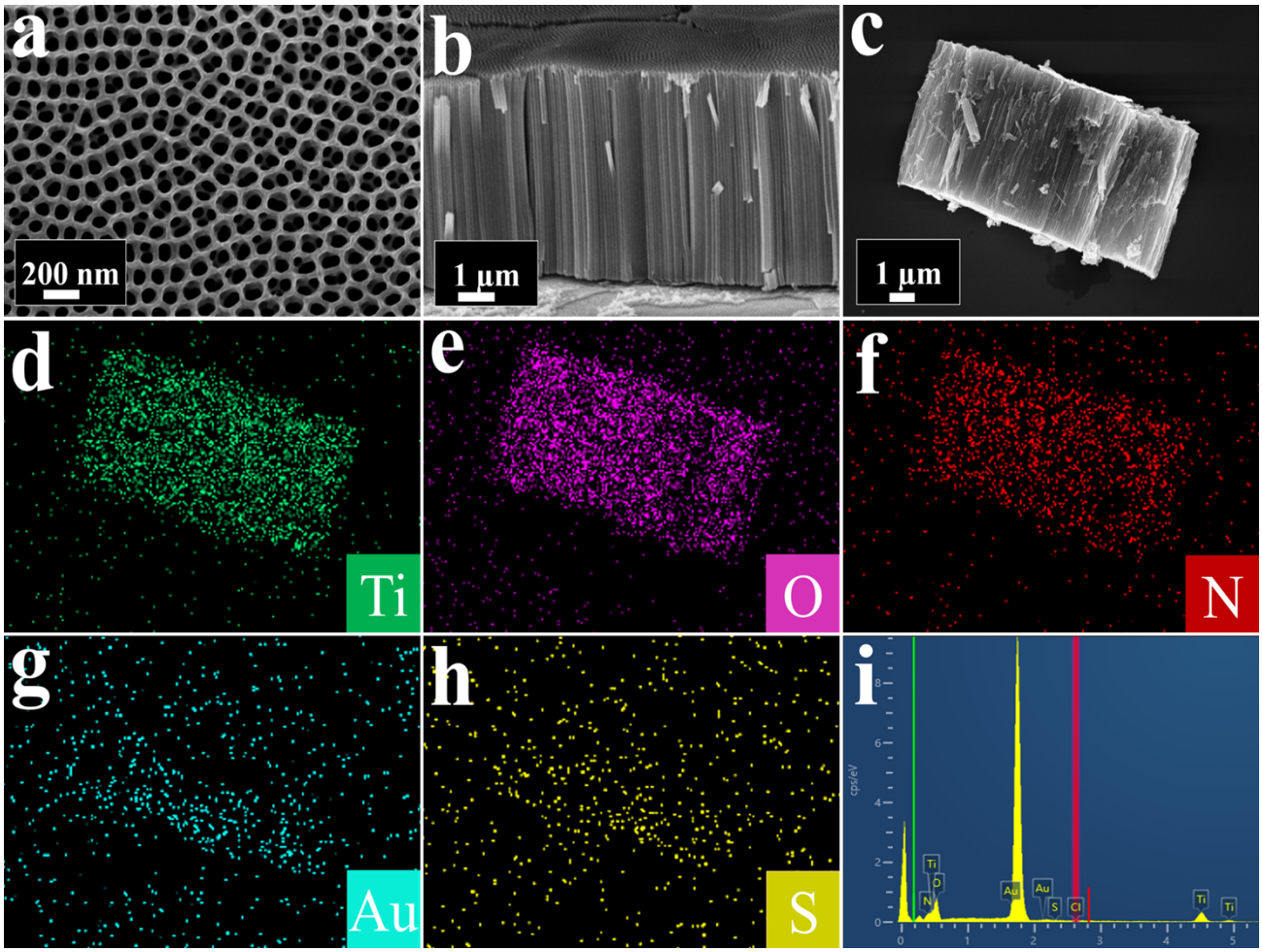

Figure S10. (a & b) Top-view and cross-sectional FESEM images of $T(Au_xP)_1$ heterostructure, (c) low-magnification FESEM image with corresponding (d-h) elemental mapping and (i) EDS results.

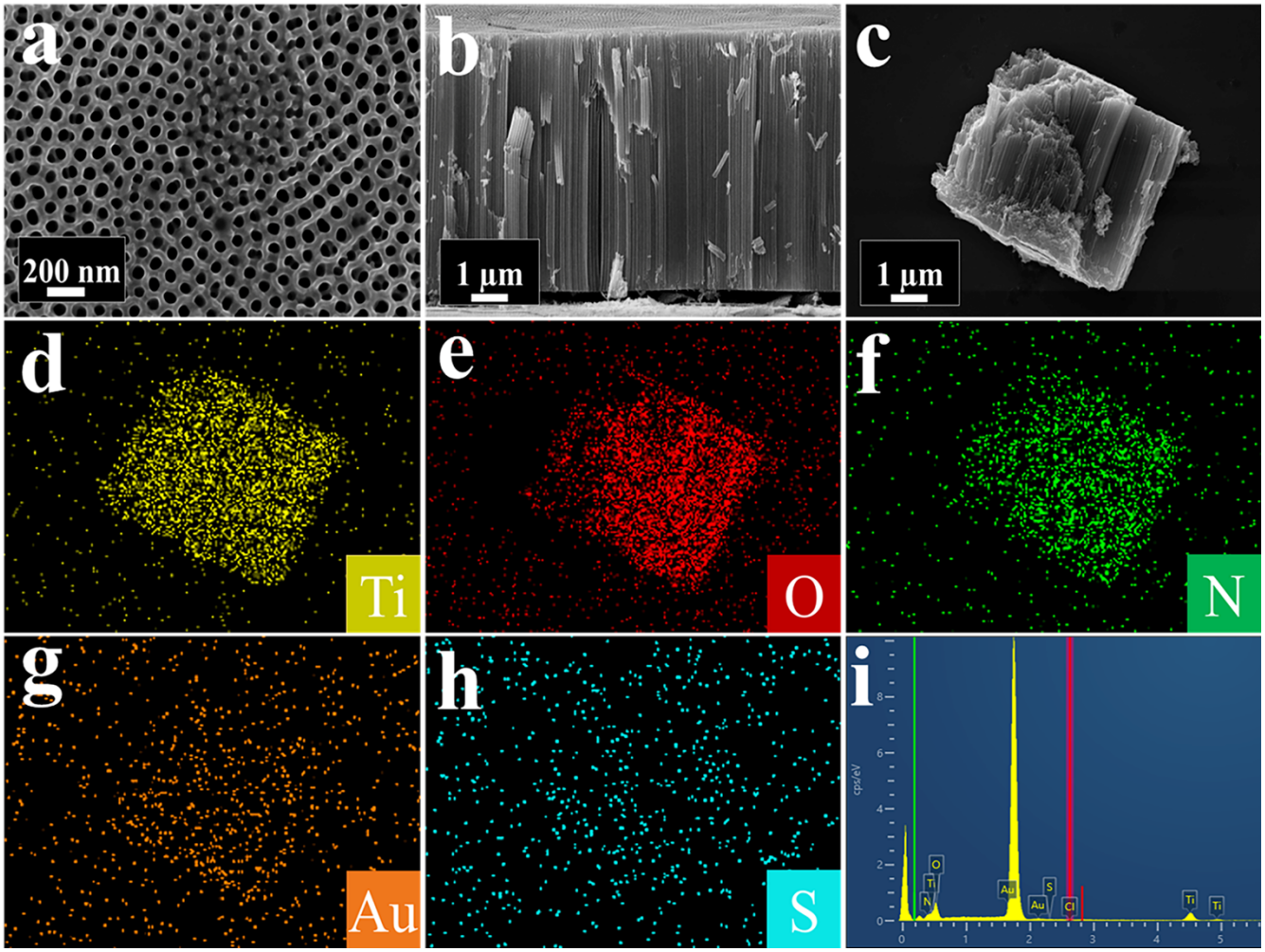

Figure S11. (a & b) Top-view and cross-sectional FESEM images of $T(Au_xP)_2$ heterostructure, (c) low-magnification FESEM image with corresponding (d-h) elemental mapping and (i) EDS results.

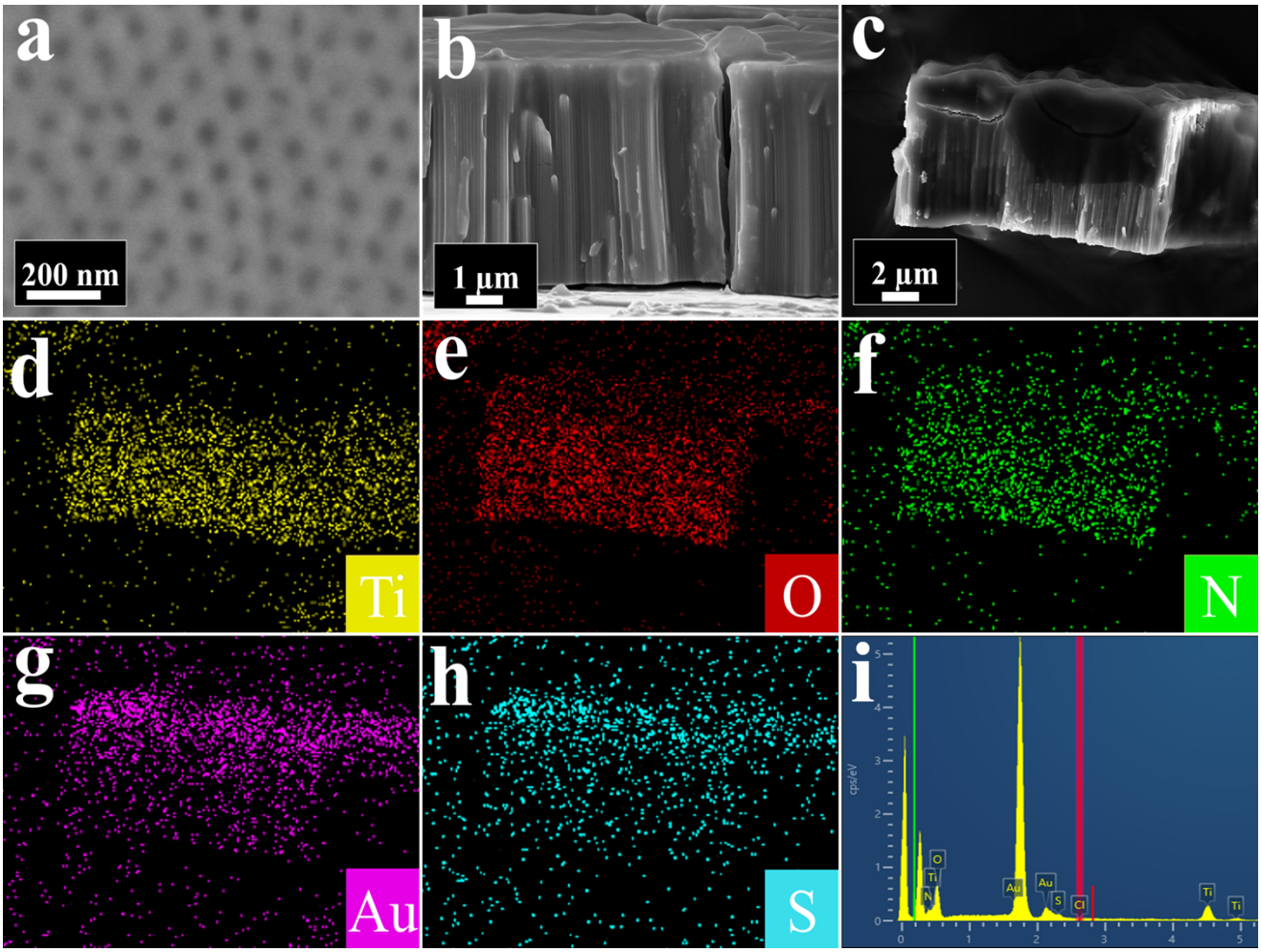

Figure S12. (a & b) Top-view and cross-sectional FESEM images of $T(Au_xP)_4$ heterostructure, (c) low-magnification FESEM image with corresponding (d-h) elemental mapping and (i) EDS results.

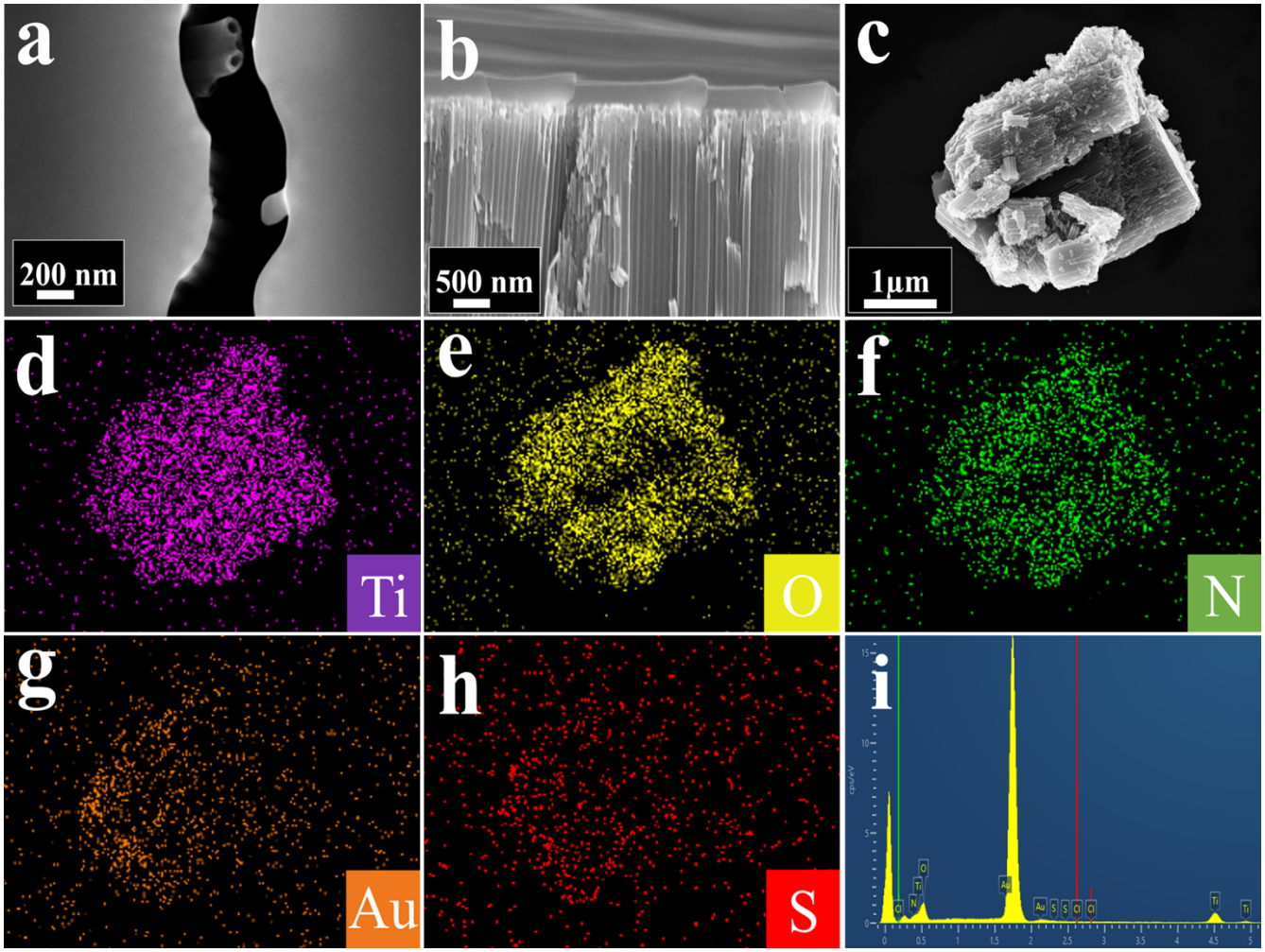

Figure S13. (a & b) Top-view and cross-sectional FESEM images of $T(Au_xP)_6$ heterostructure, (c) low-magnification FESEM image with corresponding (d-h) elemental mapping and (i) EDS results.

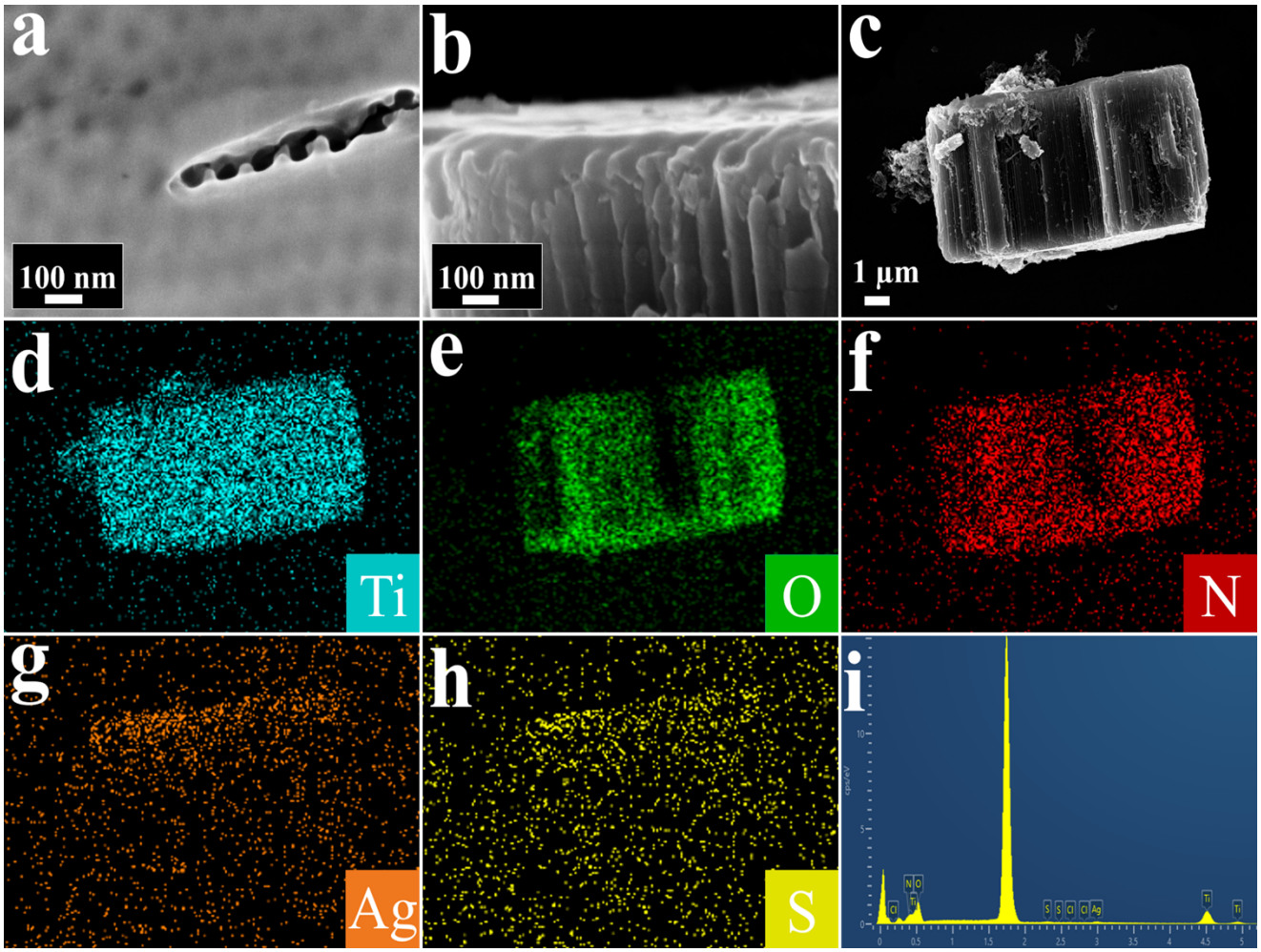

Figure S14. (a & b) Top-view and cross-sectional FESEM images of $T(Ag_xP)_8$ heterostructure, (c) low-magnification FESEM image with corresponding (d-h) elemental mapping and (i) EDS results.

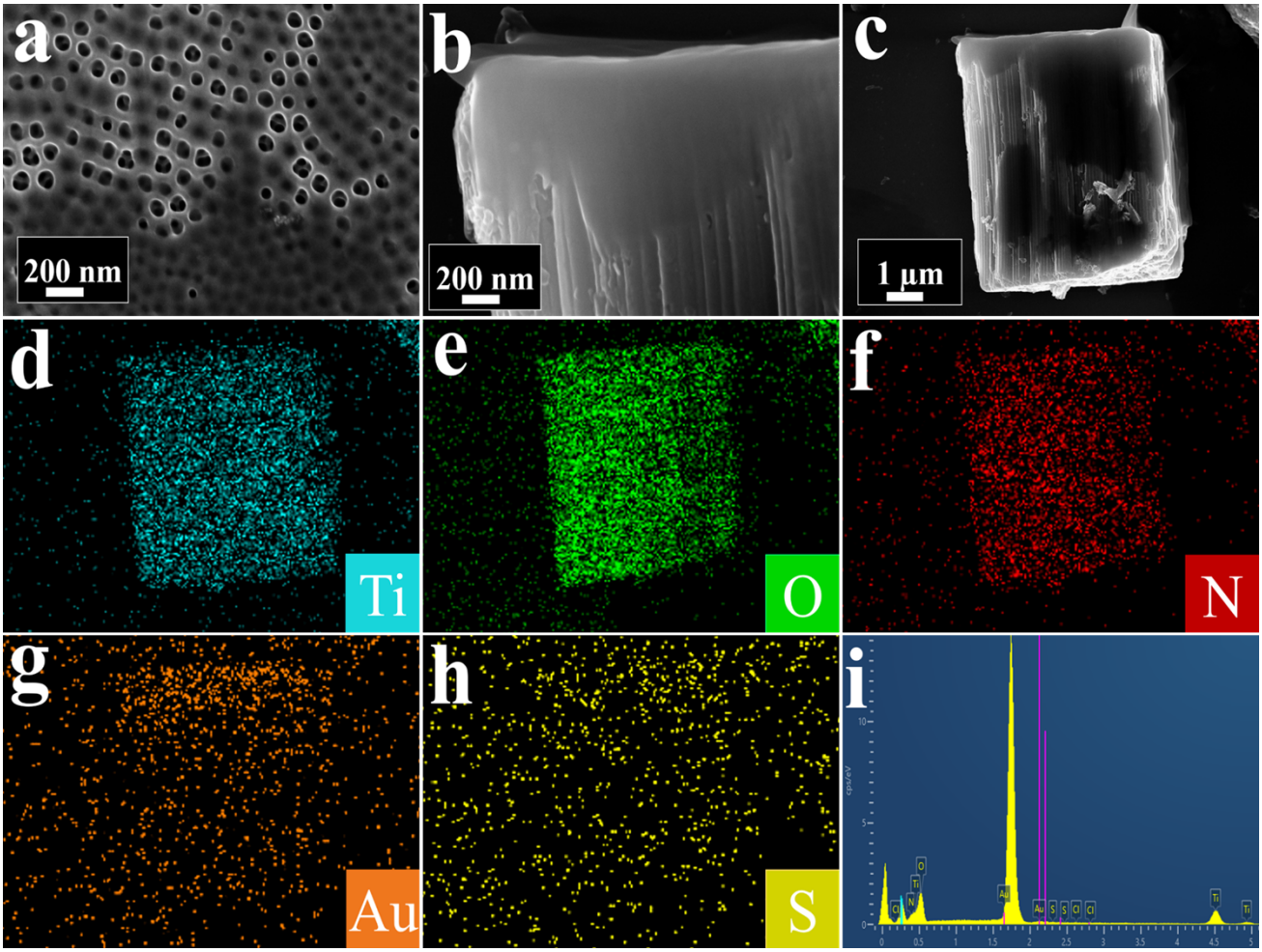

Figure S15. (a & b) Top-view and cross-sectional FESEM images of $T(Au_{25}P)_8$ heterostructure, (c) low-magnification FESEM image with corresponding (d-h) elemental mapping and (i) EDS results.

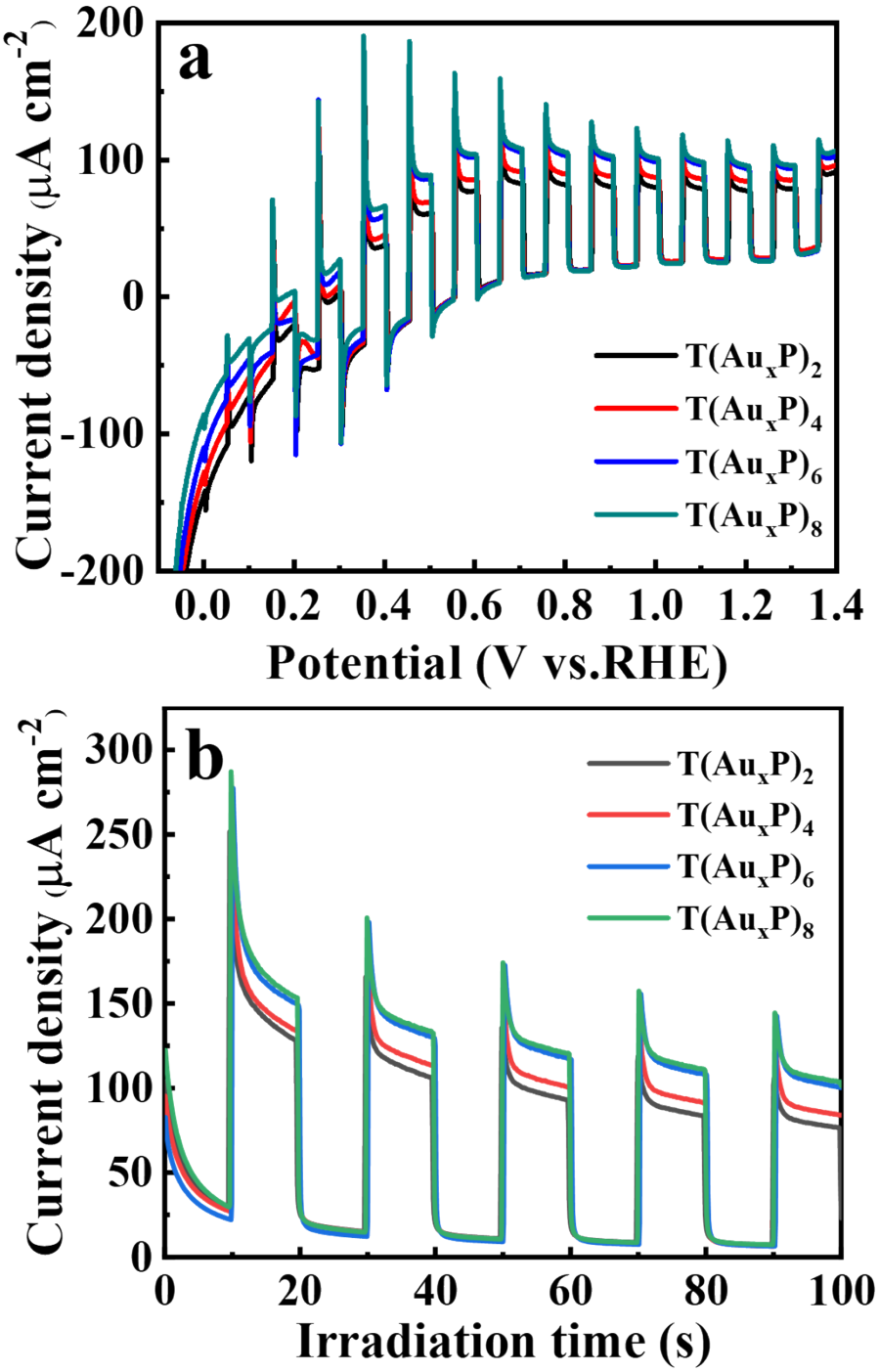

Figure S16. (a) LSV curves and (b) transient photocurrent responses of $T(Au_xP)_2$, $T(Au_xP)_4$, $T(Au_xP)_6$, and $T(Au_xP)_8$.

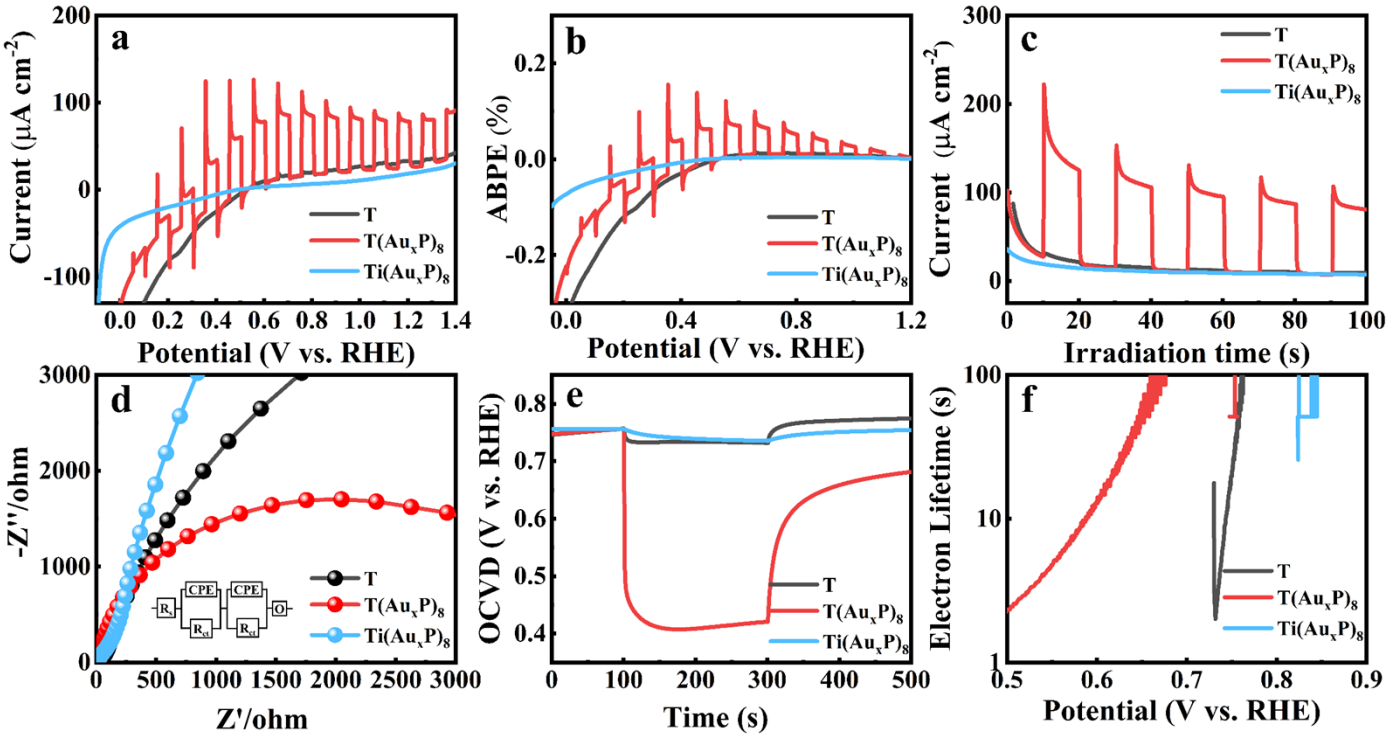

Figure S17. (a) LSV results (scan rate: 5 mV s-1) with (b) ABPE results, (c) transient photocurrent responses (bias: 1.23 V vs. RHE), (d) EIS Nyquist plots (amplitude: 10 mV, frequency: 100 kHz ~ 0.1 Hz), (e) OCVD results with (f) average electron lifetime of TNTAs, $T(Au_xP)_8$, and $Ti(Au_xP)_8$.

Note: $Ti(Au_xP)_8$, which was fabricated by direct alternate deposition of Au_x NCs and PAH on the Ti foil, shows almost negligible photocurrent (**Figure S17a-c**), which is due to the rapid electron-hole recombination over Au_x NCs. Note that $T(Au_xP)_8$ demonstrates the optimal photocurrent intensity, which is approximately 30 times higher than that of blank TNTAs under visible light irradiation. The results imply that the energy level configuration formed between Au_x NCs and TNTAs (TiO_2) is beneficial for promoting the interfacial charge transfer/separation, thus enhancing the photocurrent of composite photoanode. Moreover, EIS results (**Figure S17d**), OCVD results (**FigureS17e**) along with electron lifetime (**Figure S17f**) all manifest the analogous trend in PEC water oxidization performances.

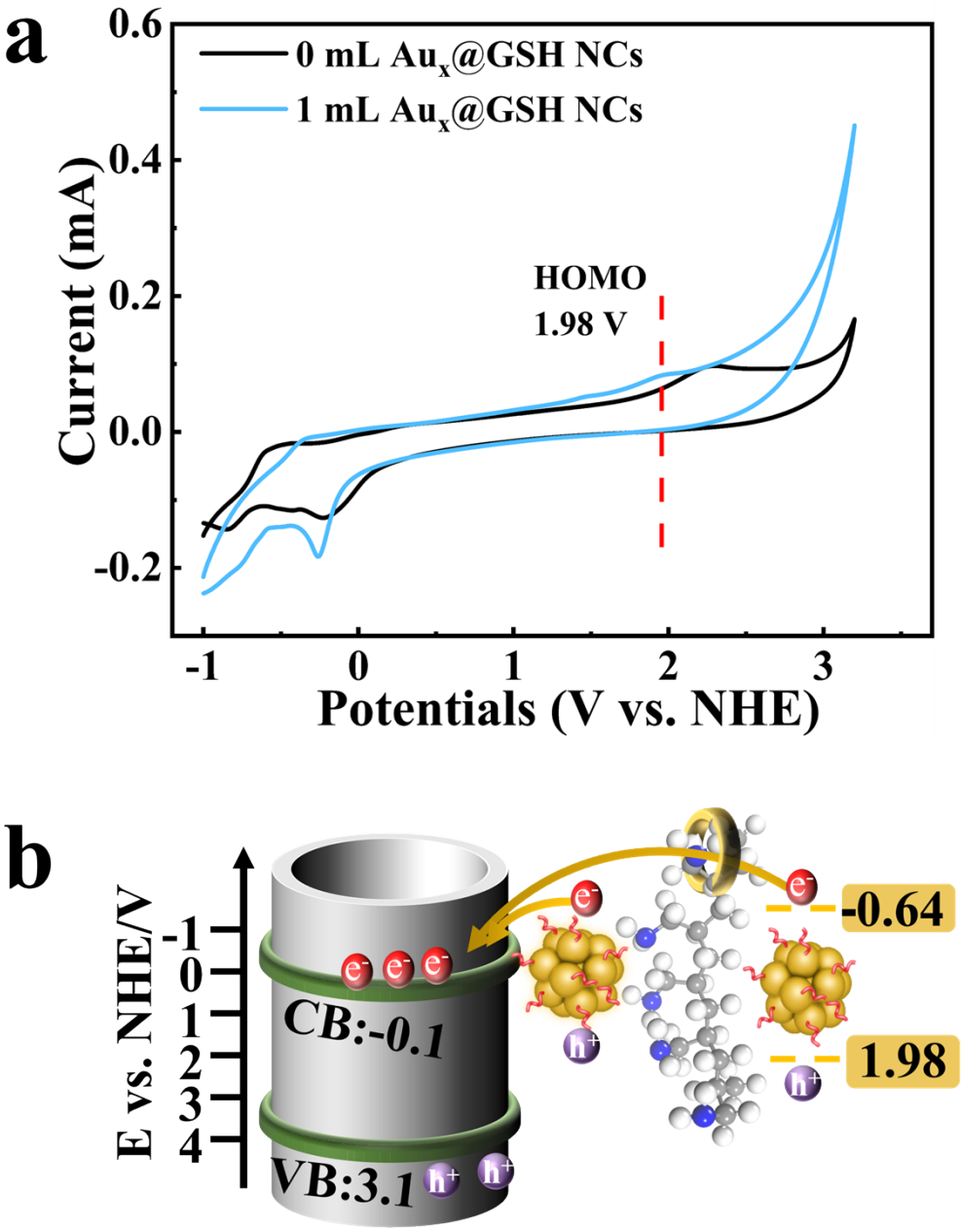

Figure S18. (a) CV results of Au_x@GSH NCs (electrolyte: degassed acetonitrile containing 0.1 M tetrabutyl ammonium perchlorate) and (b) energy level position.

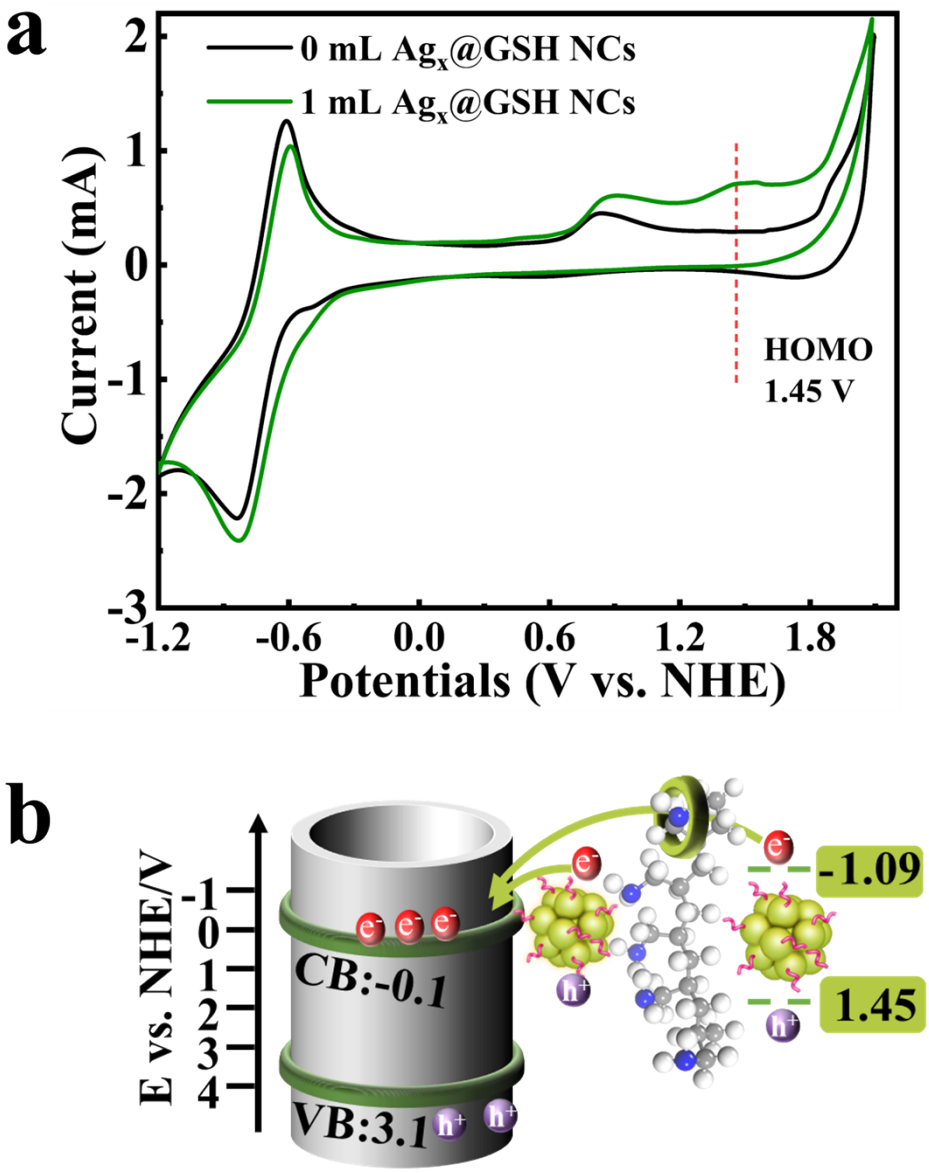

Figure S19. (a) CV results of Ag_x@GSH NCs (electrolyte: degassed acetonitrile containing 0.1 M tetrabutyl ammonium perchlorate) and (b) energy level position.

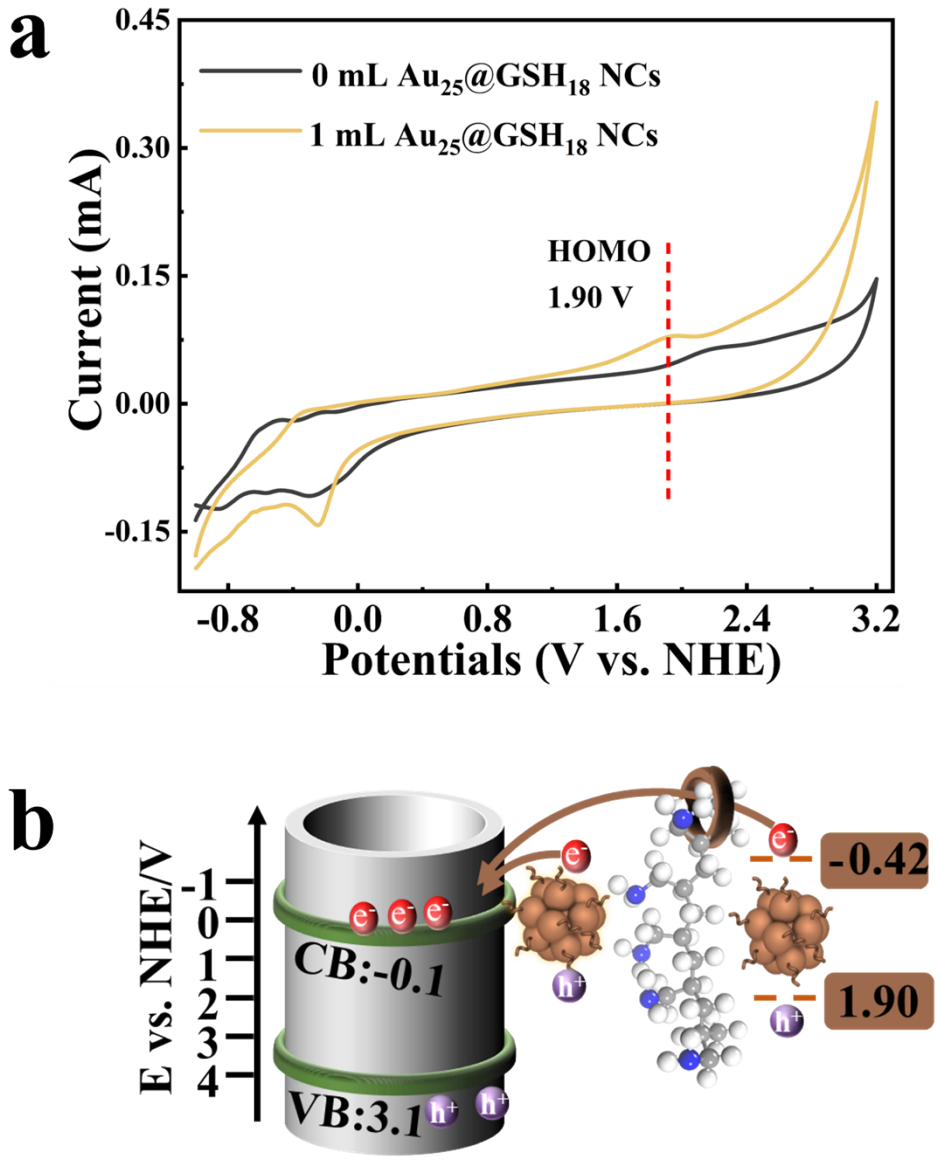

Figure S20. (a) CV results of $Au_{25}@(GSH)_{18}$ NCs (electrolyte: degassed acetonitrile containing 0.1 M tetrabutyl ammonium perchlorate) and (b) energy level position.

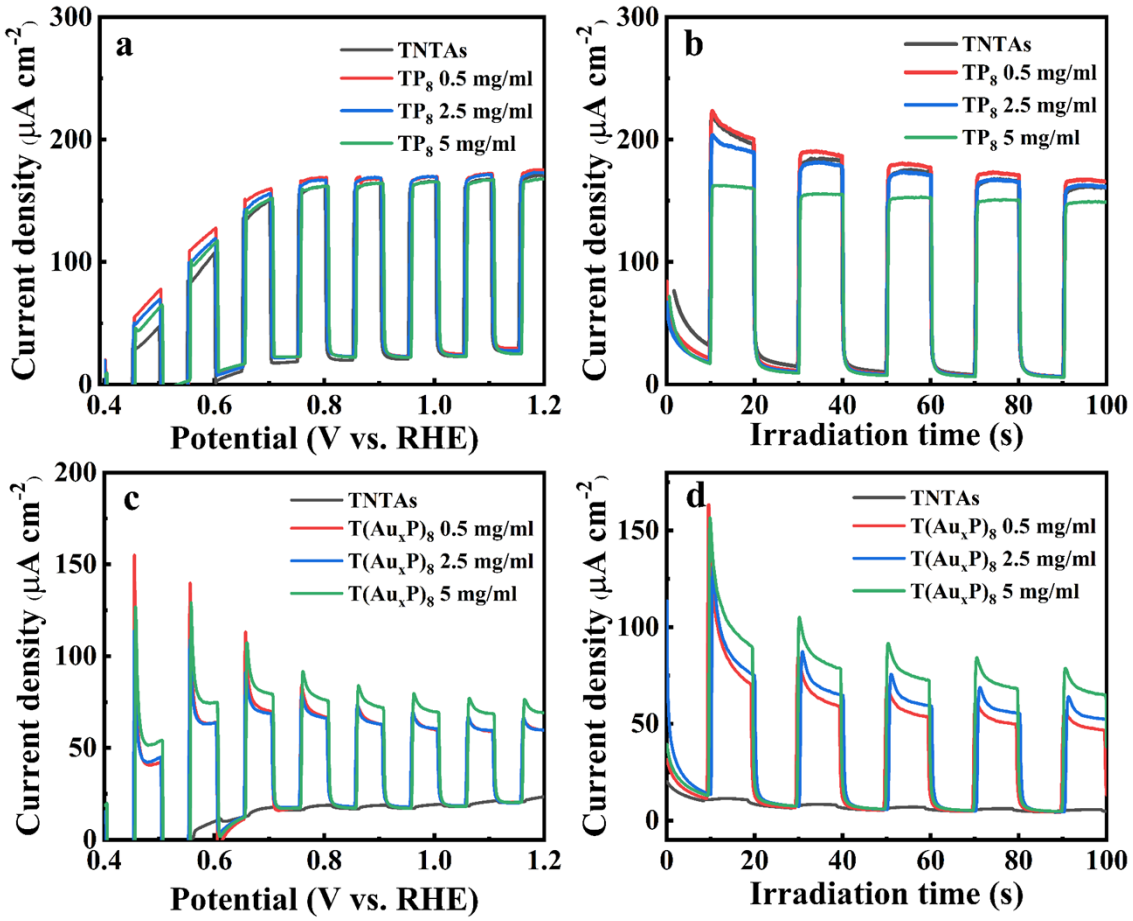

Figure S21. (a) LSV (scan rate: 5 mV s^{-1}) and (b) transient photocurrent responses (bias: 1.23 V vs. RHE) of TNTAs and TP_8 with different PAH concentration under simulated solar light irradiation (AM 1.5G); (c) LSV (scan rate: 5 mV s^{-1}) and (d) transient photocurrent responses (bias: 1.23 V vs. RHE) of TNTAs and $T(Au_xP)_8$ with different concentrations of PAH under visible light irradiation ($\lambda > 420$ nm).

Peak position (cm^{-1})	$T(Au_xP)_8$	TNTAs
3405	ν_{N-H} and ν_{O-H}	ν_{O-H} [4]
2919	ν_{C-H}	N.D. [5]
2852	ν_{C-H}	N.D. [5]
1639	δ_{N-H} and δ_{O-H} and $\delta_{C=O}$	δ_{O-H} [6]
1390	δ_{Ti-O}	δ_{Ti-O} [4]
1112	δ_{Ti-O}	δ_{Ti-O} [4]

Table S1. Peak position with corresponding functional groups for $T(Au_xP)_8$ and TNTAs.

N.D.: Not Detected.

ν: Stretching vibration.

δ: Deformation vibration.

Table S2. Chemical bond species vs. B.E. for different photoelectrodes.

Element	$T(Au_xP)_8$	TNTAs	Chemical Bond Species
C 1s A	284.60	284.6	C-C/C-H [4]
C 1s B	285.75	286.2	C-OH/C-O-C [4]
C 1s C	287.40	288.1	Carboxyl (-COO-) [4]
Ti $2p_{3/2}$ A	457.93	458.4	Anatase (4^+) [4]
Ti $2p_{1/2}$ B	464.86	464.1	Anatase (4^+) [4]
O 1s A	530.62	529.47	Lattice Oxygen [5]
O 1s B	531.60	531.13	Ti-OH [5]
O 1s C	533.65	N.D.	O–C–O [5]
N 1s A	399.16	N.D.	-NH-/-NH_2- [6, 7]
N 1s B	400.92	N.D.	-NH_3^+ [6, 7]
Au $4f_{7/2}$	83.74	N.D.	Metallic Au^0 [8]
Au $4f_{5/2}$	87.37	N.D.	Metallic Au^0 [8]
Au $4f_{7/2}$	84.45	N.D.	Au^+ [8]
Au $4f_{5/2}$	88.03	N.D.	Au^+ [8]
S $2p_{3/2}$	162.45	N.D.	-SH [9]
S $2p_{1/2}$	163.60	N.D.	-SH [9]

N.D.: Not Detected.

Table S3. Fitted EIS results of photoanodes under under visible light irradiation (λ > 420 nm) based on the equivalent circuit.

Photoanodes	R_s/ohm	R_{ct}/ohm	CPE/(F·cm^{-2})
TNTAs	3.212	11510	0.0005482
TP_8	2.685	11170	0.0004695
$T(Au_xP)_8$	3.501	3290	0.0005788
$T(Ag_xP)_8$	3.451	3375	0.0004752
$T(Au_{25}P)_8$	3.11	4233	0.0005777
$Ti(Au_xP)_8$	4.952	51370	0.0001442

Note: The inset is the equivalent circuit, where Rs is the solution resistance, CPE refers to the constant phase element, Rct indicates the charge transfer resistance at the electrode/electrolyte interface.[5] $T(Au_xP)_8$ demonstrated the smallest Rct compared with other counterparts under under visible light irradiation (λ > 420 nm), indicative of its lowest interfacial charge transfer resistance.

Table S4. The bandgap, HOMO and LUMO levels of Au_x@GSH, Ag_x@GSH, and Au_{25}@$(GSH)_{18}$ NCs.

Metal NCs	Bandgaps (eV)	HOMO (eV vs. NHE)	HOMO (eV vs. NHE)
Au_x@GSH	2.62	1.98	−0.64
Ag_x@GSH	2.54	1.45	−1.09
Au_{25}@$(GSH)_{18}$	2.32	1.90	−0.42

Note: LUMO level is determined by bandgap and HOMO level, among which bandgap is determined by the UV−vis absorption spectrum and HOMO level is determined by CV results.

References

[1] Hou, S.;Dai, X.-C.;Li, Y.-B.;Huang, M.-H.;Li, T.;Wei, Z.-Q.;He, Y.;Xiao, G.; Xiao, F.-X. Charge transfer modulation in layer-by-layer-assembled multilayered photoanodes for solar water oxidation. *J. Mater. Chem. A* **2019**, *7*, 22487-22499.

[2] Dai, X. C.;Huang, M. H.;Li, Y. B.;Li, T.;Hou, S.;Wei, Z. Q.; Xiao, F. X. Probing the Advantageous Photosensitization Effect of Metal Nanoclusters over Plasmonic Metal Nanocrystals in Photoelectrochemical Water Splitting. *J. Phys. Chem. C* **2020**, *124*, 4989-4998.

[3] Yuan, X.;Setyawati, M. I.;Tan, A. S.;Ong, C. N.;Leong, D. T.; Xie, J. P. Highly luminescent silver nanoclusters with tunable emissions: cyclic reduction-decomposition synthesis and antimicrobial properties. *NPG Asia Mater.* **2013**, *5*, 8.

[4] Hou, S.;Mo, Q. L.;Zhu, S. C.;Li, S.;Xiao, G.; Xiao, F. X. Precisely Modulating the Photosensitization Efficiency of Transition-Metal Chalcogenide Quantum Dots toward Solar Water Oxidation. *Inorg. Chem.* **2022**, *61*, 1188-1194.

[5] Wei, Z. Q.;Dai, X. C.;Hou, S.;Li, Y. B.;Huang, M. H.;Li, T.;Xu, S.; Xiao, F. X. Branched polymer-incorporated multi-layered heterostructured photoanode: precisely tuning directional charge transfer toward solar water oxidation. *J. Mater. Chem. A* **2020**, *8*, 177-189.

[6] Wei, M.;Xie, Z. Y.;Sun, L. G.; Gu, Z. Z. Electrochemical Properties of a Boron-Doped Diamond Electrode Modified with Gold/Polyelectrolyte Hollow Spheres. *Electroanalysis* **2009**, *21*, 138-143.

[7] Goh, S. H.;Lee, S. Y.;Zhou, X.; Tan, K. L. X-ray photoelectron spectroscopic studies of interactions between poly(4-vinylpyridine) and poly(styrenesulfonate) salts. *Macromolecules* **1998**, *31*, 4260-4264.

[8] Weng, B.;Lu, K. Q.;Tang, Z.;Chen, H. M.; Xu, Y. J. Stabilizing ultrasmall Au clusters for enhanced photoredox catalysis. *Nat. Commun.* **2018**, *9*, 1543.

[9] Nguyen, T. T. T.;Belbekhouche, S.;Dubot, P.;Carbonnier, B.; Grande, D. From the functionalization of polyelectrolytes to the development of a versatile approach to the synthesis of polyelectrolyte multilayer films with enhanced stability. *J. Mater. Chem. A* **2017**, *5*, 24472-24483.